Science of the Total Environment 927 (2024) 172144

Contents lists available at ScienceDirect

Science of the Total Environment

journal homepage: www.elsevier.com/locate/scitotenv

The role of hydraulic conductivity in the Pine Island Glacier's subglacial water distribution

Yufang Zhang [a], John C. Moore [b,*], Liyun Zhao [a,*], Mauro A. Werder [c,d], Rupert Gladstone [b], Michael Wolovick [e]

[a] State Key Laboratory of Earth Surface Processes and Resource Ecology, Faculty of Geographical Science, Beijing Normal University, 100875, China
[b] Arctic Centre, University of Lapland, 96101 Rovaniemi, Finland
[c] Laboratory of Hydraulics, Hydrology and Glaciology (VAW), ETH Zurich, Zurich, Switzerland
[d] Swiss Federal Institute for Forest, Snow and Landscape Research (WSL), Birmensdorf, Switzerland
[e] Glaciology Section, Alfred-Wegener-Institut Helmholtz-Zentrum für Polar- und Meeresforschung, Bremerhaven, Germany

HIGHLIGHTS

- Subglacial channels extending for 100-200 km and a small swamp beneath Pine Island Glacier was simulated
- Water pressure builds up to 84% of ice overburden pressure in channelized region
- Tipping point behavior was found for the basal hydraulic conductivity parameter
- Sheet system may cause opening of effecient drainage channels

GRAPHICAL ABSTRACT

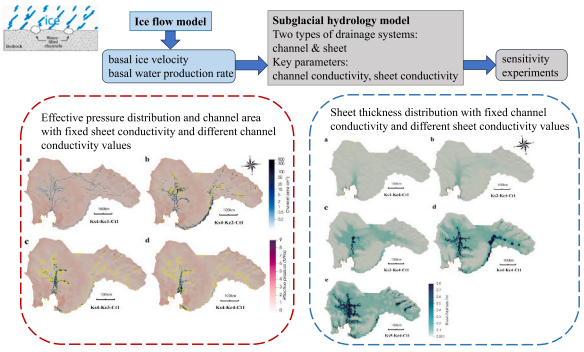

ARTICLE INFO

Editor: Christian Herrera

Keywords:
Hydrology modelling
Antarctic glacier
Subglacial hydrology
Basal conductivity
Pine Island Glacier
Glacier drainage model

ABSTRACT

Global climate warming leads to ever-increasing glacier mass loss. Pine Island Glacier in Antarctica is one of the largest contributors to global sea level rise (SLR). One of the biggest uncertainties in the assessment of glacier contribution to SLR at present are subglacial hydrology processes which are less well known than other ice dynamical processes. We use the Glacier Drainage System (GlaDS) model which couples both distributed and channelized components to simulate the basal hydrology of Pine Island Glacier with basal sliding and meltwater production taken from a full-Stokes Elmer/Ice model fitting observed surface velocities. We find ≈100 km long Rothlisberger channels up to 26 m in diameter extending up glacier from the grounding line along the main trunk of Pine Island Glacier delivering 51 $m^3\ s^{-1}$ of fresh water to the grounding line. Channelization occurs at high water pressure because of high basal melt rates (maximum of 1 m a^{-1}) caused by high rates of shear heating in regions with fast ice flow (>1000 m a^{-1}). We simulate a shallow "swamp" of 0.8 m water depth where flow transitions from a distributed system into the channels. We performed a set of 38 sensitivity experiments varying sheet and channel conductivity over 4 orders of magnitude. We find a threshold behavior in distributed sheet conductivity above which basal water pressures are unaffected by changing channel conductivities. Our findings

* Corresponding authors.
E-mail addresses: john.moore.bnu@gmail.com (J.C. Moore), zhaoliyun@bnu.edu.cn (L. Zhao).

https://doi.org/10.1016/j.scitotenv.2024.172144
Received 18 December 2023; Received in revised form 5 March 2024; Accepted 30 March 2024
Available online 4 April 2024

suggest a strong need to better understand controls on basal water conductivity through the distributed system. This issue is critical to improve model-based predictive capability for the Pine Island Glacier and, more generally, the Antarctic Ice Sheet.

1. Introduction

Accelerating glacier mass loss in recent years has caused concern as they are a direct indicator of global warming (Wu et al., 2021). The Sixth Assessment Report of the Intergovernmental Panel on Climate Change (IPCC AR6) highlights the importance of glacier dynamics impacts on global sea level rise. Subglacial water plays a significant role in ice flow, but is difficult to incorporate into ice dynamics models (Stearns et al., 2008). Mutual feedback between the ice dynamics and basal hydrological systems occurs because (a) basal water pressure impacts glacier sliding, (b) the sliding rate dictates the drainage space evolution, and (c) the frictional heat generated by basal sliding can melt the ice providing input to the hydrological system that then impacts the local friction and basal sliding speeds (e.g. De Fleurian et al., 2018). Direct observation of subglacial drainage using borehole (e.g. Andrews et al., 2014), dye-tracing tests (e.g. Cowton et al., 2013) and radar sounding (e.g. Chu et al., 2016; Siegert et al., 2016) are helpful to understand the basal conditions, but such measurements are difficult, sparse, and isolated, limiting our comprehension of spatial and temporal change in the subglacial hydrology system. Channels beneath various Antarctic glaciers have been inferred on the basis of radar sounding of the basal reflection characteristics on the grounded ice sheet (Schroeder et al., 2013, 2015; Dow et al., 2020, 2022; Huang et al., 2024). These channel systems typically extend some hundred km inland from the grounding line. Channels were directly observed by radar under the floating Filchner–Ronne (Le Brocq et al., 2013) and Roi Baudouin Ice Shelves (Drews et al., 2017), with the inference that a channelized drainage system fed them from beneath the inland grounded ice sheet.

Various attempts have been made to develop basal hydrology models over the past decades. With the development of computer power, hydrology simulations have been extended from one-dimensional flow-line models (e.g. Flowers et al., 2004) to two dimensional models at the basal plane (e.g. Schoof, 2010; Hewitt, 2011; Werder et al., 2013).

The two-dimensional Glacier Drainage System (GlaDS) model (Werder et al., 2013) couples a distributed water sheet model - a continuum description of a linked cavity drainage system (Hewitt, 2011) - with a channelized water flow model, modelled as Röthlisberger channels (R-channels) (Nye, 1976; Röthlisberger, 1972). GlaDS has been widely applied, for instance to Alpine glaciers (Werder et al., 2013) and Recovery Ice Stream in Antarctica with idealized basal topography (Dow et al., 2018a,b, 2020). GlaDS can be used with basal ice velocity and water flux inputs from an ice sheet model, to provide a steady state solution for hydraulic variables. It can also be coupled to an ice sheet model to simulate the evolution of the subglacial drainage system. Gagliardini and Werder (2018) coupled GlaDS to a prognostic ice flow model to study the impact of surface melt reaching the bed through surface crevassing on ice flux on a synthetic Greenland margin-like setup.

Other modelling frameworks have also been developed: CUAS (confined–unconfined aquifer system) is an equivalent single-layer hydrology model (Beyer et al., 2018) containing parameterizations for both efficient and inefficient drainage which consider porous medium conditions. Beyer et al. (2018) claim, CUAS provides more realistic velocities for ice dynamics model they used in the coastal region. The MPAS (Model for Prediction Across Scales)-Albany Land Ice model (Hager et al., 2022) is a conceptual model constructed on Voronoi grid with many approximations, such as neglecting the pressure-dependent melting/freezing process. The SHAKTI (Subglacial Hydrology And Kinetic, Transient Interactions) model (Sommers et al., 2023) is a highly simplified model where cavity opening by sliding, englacial storage and melt due to changes in the pressure-melting-point temperature are all neglected. Among these recently developed and hydrology models, the GlaDS framework is probably the most sophisticated approach available.

Pine Island Glacier (PIG) is one of the largest outlets in the Amundsen Sea Sector of West Antarctica, with flow speeds in excess of 3000 m a^{-1} and it has the potential to raise global sea level significantly on centennial timescales (Rignot et al., 2019). PIG lost 2720 ± 1390 Gt at an average rate of 109 ± 56 Gt a^{-1} over the period 1992–2017 (Shepherd et al., 2018). The PIG grounding line intermittently retreated about 20 km from 1996 to 2009 (Joughin et al., 2010), and lost about 11,500 km^2 of grounded ice area from 2009 to 2017 (Rignot et al., 2022). Many processes contributed to this large ice loss, with subglacial hydrology potentially being one of the most important ones as it controls basal sliding velocity but it also one of least constrained processes. Basal water pressures impact friction and directly influence ice flow and ice discharge to the ocean (Dow et al., 2022). Therefore, we aim to analyze PIG's subglacial hydrologic system and how it may potentially impact ice dynamics.

In this study, we make a sensitivity analysis using the GlaDS model to simulate PIG subglacial hydrology with a range of prescribed water channel and water sheet properties with fixed simulated ice dynamics and examine the distribution of different hydrological elements. We firstly introduce the model implementation, boundary conditions, inversion method used to give basal conditions, and describe parameters we choose to vary. We spin-up the model and run it to steady-state to examine the hydrologic spatial pattern. Then, we explore the sensitivity of the modelled subglacial hydrology system to channel and sheet conductivities.

2. The GlaDS model

GlaDS integrates both the inefficient drainage system, made up of a distributed water sheet consisting of linked cavities, and an efficient drainage system of channelized water flow components. A full description and equations are given in Werder et al. (2013). Here, we briefly introduce the model.

The hydraulic potential at the bed is defined by

$$\phi = \phi_m + p_w, \tag{1}$$

where p_w is the water pressure, with the elevation potential

$$\phi_m = \rho_w g B, \tag{2}$$

in which ρ_w is water density, g is gravitational acceleration, and B is the bed elevation. The effective pressure, N, is defined as $N = p_i - p_w$, where p_i is the ice overburden pressure.

Numerically, the whole domain is partitioned into subdomains to allow parallel computations. Channel segments exchange water with each other at the network nodes, and exchange water along their length with the sheet in the adjacent subdomains. Water exchange at each network node and along segments is set by mass conservation. In practice as the model elements are relatively small and the channels are free to evolve at each time step, the position, length and cross-section of channels is not prescribed by the model mesh or spatial resolution.

The sheet equations are given by:

$$\frac{e_v}{\rho_w g}\frac{\partial \phi}{\partial t} + \nabla \cdot q + w - v - m = 0, \tag{3}$$

$$\frac{\partial h}{\partial t} = w - v \tag{4}$$

where e_v is the englacial void ratio, $e_v\frac{\phi-\phi_m}{\rho_w g}$ is the stored volume per unit area of bed, h is the water sheet thickness, $\boldsymbol{q}$ is the discharge in distributed system given by

$$\boldsymbol{q} = -k_s h^{\alpha_s}|\nabla\phi^{\beta_s-2}|\nabla\phi \tag{5}$$

where k_s is sheet conductivity, taken as a constant, the sheet flow exponent α_s is set to 1.25 and β_s to 1.5 which corresponds to fully turbulent flow in the empirical Darcy-Weisbach law. The time rate of change for h is determined by the rate of opening and closing of a cavity. The rate of cavity opening, w, is given by

$$w(h) = \begin{cases} u_b(h_r - h), h < h_r \\ 0, otherwise \end{cases} \tag{6}$$

where h_r is the typical bedrock bump height and l_r the typical cavity spacing, u_b is basal sliding speed. The opening rate of the cavity caused by sliding over a bump is proportional to the sliding speed. The cavities close by viscous ice deformation depending on the effective pressure N. The rate of cavity closing, v, is given by

$$v(h,N) = \widetilde{A}h|N^{n-1}|N \tag{7}$$

where $\widetilde{A}$ is the rheological constant of ice multiplied by an order-one geometrical factor that depends on the shape of cavities, and n is the exponent in Glen's law.

The channels are governed by equations on the channel edges:

$$\frac{\partial Q}{\partial s} + \frac{\partial S}{L}\left(\frac{1}{\rho_i} - \frac{1}{\rho_w}\right) - \nu_c - m_c = 0, \tag{8}$$

$$\frac{\partial S}{\partial t} = \frac{\Xi - \Pi}{\rho_i L} - \nu_c, \tag{9}$$

where Q is the channel discharge, S is the channel cross-sectional area, s is the horizontal coordinate along the channel, ρ_i is ice density, L is the latent heat of fusion, $\frac{\Xi-\Pi}{\rho_i L}$ represents opening rate of the channel, ν_c is the closure rate of the channel, and m_c is water entering the channel from the surrounding distributed system. The channel discharge, Q, is related to the gradient of hydraulic potential, ϕ, via a turbulent flow parameterization:

$$Q = -k_c S^{\alpha_c}\left|\nabla\frac{\partial\phi}{\partial s}\right|^{\beta_c-2}\frac{\partial\phi}{\partial s} \tag{10}$$

where k_c is channel conductivity, taken as a constant. The channel flow exponents, α_c and β_c take constants the same as in Werder et al. (2013) with the sheet flow exponents assuming fully turbulent flow. The dissipation rate of potential energy, Ξ, is given by

$$\Xi = \left|Q\frac{\partial\phi}{\partial s}\right| + \left|l_c q_c \frac{\partial\phi}{\partial s}\right|, \tag{11}$$

where the first term represents the contribution from the water flowing in the channel, and the second term from the water flowing in a width l_c of the sheet lying underneath the channel and $q_c = -k_s h^{\alpha_s}\left|\frac{\partial\phi}{\partial s}\right|^{\beta_s-2}\frac{\partial\phi}{\partial s}$ approximates the discharge in the sheet flowing in the direction of the channel.

The water is assumed to be at the pressure melting point, so change in water pressure leads to melting or refreezing at the rate $-\Pi/\rho_i L$. The sensible heat change of the water, Π, is given by

$$\begin{aligned}\Pi &= -c_t c_w \rho_w (Q + f l_c q_c)\frac{\partial P_w}{\partial s} \\ &= -c_t c_w (Q + f l_c q_c)\frac{\partial}{\partial s}(\phi - \phi_m)\end{aligned} \tag{12}$$

where c_t is the Clapeyron slope or pressure melting coefficient, c_w is the specific heat capacity of water, and f is a logical parameter to guarantee the contribution of the sheet flow to refreezing is conditional on positive channel size:

$$f = \begin{cases} 1, if S > 0 \vee q_c\frac{\partial p_w}{\partial s} > 0 \\ 0, otherwise \end{cases}, \tag{13}$$

The closure rate of the channel, ν_c, due to viscous creep is

$$\nu_c(S,N) = \widetilde{A_c}S|N|^{n-1}N \tag{14}$$

where $\widetilde{A_c}$ is the rheological constant for ice multiplied by an order-one factor that depends on the cross-sectional geometry of the channel. Model parameter values are given in Table 1 and follow the same nomenclature as in Werder et al. (2013).

3. Experiments

GlaDS requires bedrock topography data and boundary conditions on ice overburden pressure, basal ice velocity, and basal water fluxes. The domain we use encompasses the whole PIG drainage basin (Willis et al., 2021). The bedrock topography (Fig. 1a) is from BedMachine Antarctica (Morlighem et al., 2019). Most of the ice bottom is below sea level. A deep trough in the center of PIG lies ~1500 m below sea level. This funnel-like geometry provides an environment for water accumulation.

The key inputs - basal ice velocity and basal water production rate come from simulations with a full-Stokes ice flow model for PIG (Gladstone and Wang, 2022) using Elmer/Ice (http://elmerice.elmerfem.org/).The modelled basal sliding speed ranged from zero upstream inland to 4300 m a^{-1} near the grounding line (Fig. 1f). The modelled basal water production rate ranged from 0.01 m a^{-1} in the slow-flowing catchment to 1 m a^{-1} near the grounding line (Fig. 1e). Basal melt rates over 0.8 m a^{-1} are concentrated in "sticky spots" located near the grounding line (Fig. 1e). Sticky spots are hard bedrock protrusions that stick out into the glacier through any deformable sediment creating a rough bed (Gladstone et al., 2014). We use the same mesh as Gladstone and Wang (2022).

We set a Dirichlet boundary condition for the hydraulic potential $\phi = 0$ at the grounding line and for the ice shelf. Channels are not allowed to open along the domain boundaries. Channels start with zero area. We set a bedrock bump height as 0.1 m representing the possible topography in real world.

We set time steps in the GlaDS model firstly grow linearly from 2.3 h to 17.52 h in 18 timesteps, then keep 17.52 h until the simulation

Table 1
Values of the parameters used in the control experiment.

Description	Variable	Value	Units
Ice flow constant	A	2.5×10^{-25}	$Pa^n s^{-1}$
Ice density	ρ_i	910	kgm^{-3}
Water density	ρ_w	1000	kgm^{-3}
Glen exponent	n	3	m s^{-2}
Gravity constant	g	9.8	
Sheet flow exponent	α_s	1.25	
Sheet flow exponent	β_s	1.5	
Channel flow exponent	α_c	1.25	
Channel flow exponent	β_c	1.5	
Sheet conductivity	k_s	10^{-3}	$m^{7/4}kg^{-1/2}$
Channel conductivity	k_c	10^{-2}	$m^{2/3}kg^{-1/2}$
Sheet width below channel	l_c	2	m
Cavity spacing	l_r	2	m
Bedrock bump height	h_r	0.1	m
Englacial void ratio	e_v	10^{-4}	
Pressure melt coefficient	c_t	7.5×10^{-8}	KPa^{-1}
Heat capacity of water	c_w	4220	$Jkg^{-1}K^{-1}$
Latent heat of fusion	L_w	3.34×10^5	Jkg^{-1}

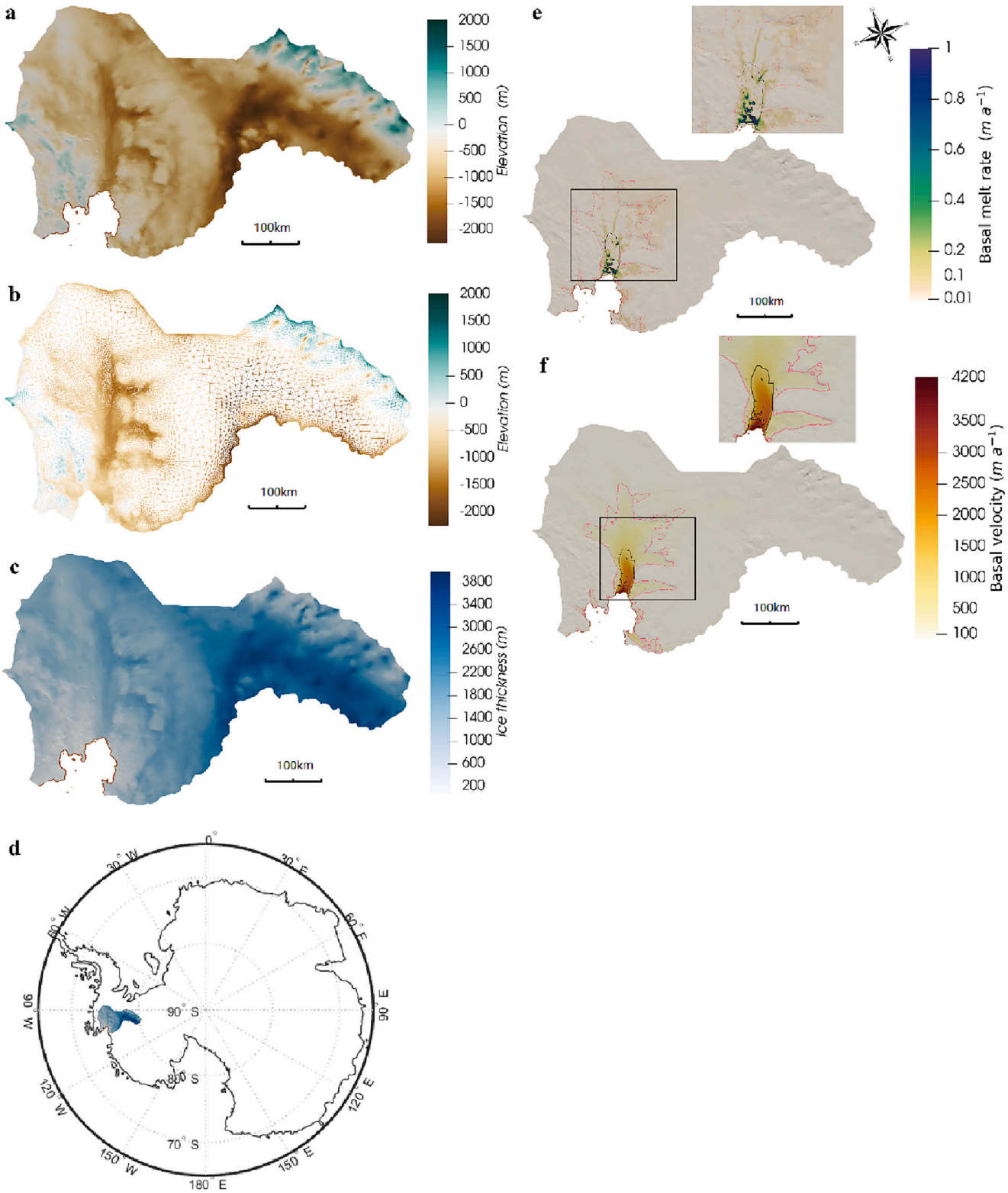

Fig. 1. (a) Bed topography from BedMachine Antarctica project (Morlighem et al., 2019); (b) the mesh used in simulations with bed topography; (c) ice thickness; (d) Antarctic location map with PIG domain in color; (e) simulated basal melt rate by Elmer/Ice model (Gladstone and Wang, 2022), with the black boxed region shown inset; (f) modelled basal velocity by Elmer/Ice model (Gladstone and Wang, 2022), with the black boxed region shown inset. Ice velocity contours of 1000 m a^{-1} and 100 m a^{-1} are plotted as black and pink curves in panels (e, f). The grounding line is plotted as a brown curve in panels a, c, e, f.

reaches steady state. Steady state is defined when the change of water depth between steps at every node is $<10^{-4}$ m. Each simulation runs for about 145 model years.

We run the simulations in parallel using the GlaDS solver (Gagliardini and Werder, 2018) of Elmer/Ice v8.2 (Zwinger et al., 2020). Model parameter values in the control run are given in Table 1. We conduct a series of sensitivity tests by varying values of basal sheet conductivity, and channel conductivity mimicking various porosities of

the basal drainage system (Table 2). As bedrock bump height and sheet conductivity have anti-correlated impact on drainage system (Brinkerhoff et al., 2021), we chose sheet conductivity value for sensitivity experiment in our study. We also do tests with two values of pressure melt coefficient (Table 2), essentially using either the known physical behavior in the control run, or removing any effects of pressure on the melting point to determine the areas of the bed where supercooling affects basal hydrology. The pressure melting point (unit: K), $T_{pmp} = 273 - C_t \times p$, depends on the pressure p, and C_t the pressure melt coefficient. One purpose of these tests is to determine the level of control that these 3 parameters have on the modelled basal hydrology system and its implications for the basal velocities, and if there is any 'tipping point' behavior. Essential parameters chosen in our sensitivity experiments can represent most behavior of hydrology model. However, not all less-constrained parameters can be examined in this study due to their large quantity.

4. Simulation results

4.1. Steady state results with the control run

The control run uses parameter values in Table 1, corresponding to parameters (k_{s3}, k_{c2}, C_{t1}) of Table 2. Scattered channels segments start to appear on elements near the PIG grounding line after 3.62 h of simulation. Sporadic channels located at element edges appear and disappear and remain disconnected during the first 9 simulation years. The channels then begin to form a connected system with one central channel, 33 km long after 14 years of evolution. The channel lengthens to 42 km after 18 years of evolution with an area of 300–500 m^2 (Fig. S1a), close to the grounding line. A dendritic channel structure with smaller area is at the inland head of the channel along the bedrock trough. After 145 years of simulation steady state is reached, and effective pressure and sheet thickness are stable. The main channel is about 130 km long (Fig. S1b).

The channel runs perpendicular to the hydropotential contours running from south-east to north-west, but there is a noticeable "dog-leg" near the 2 MPa hydraulic potential contour (Fig. S1a, b). In general the channel lies in the central trough with bed elevations 1000–1800 m below sea level with ice flow speed over 1000 m a^{-1} within the 2–5 MPa hydraulic potential contours. The highest basal melt rates (Fig. 1e; 0.6^{-1} m a^{-1}) are near the grounding line end of the channel.

The steady state distribution of subglacial hydrological variables in the control run is plotted in Fig. 2. The highest water pressures (>21 MPa) are in the southern part of PIG (Fig. 2a), but there are also relatively high pressures along the central trunk (10–21 MPa; Fig. 2a). The high water pressures in the southern part of PIG are due to very thick ice (>3800 m, Fig. 1c) and deep bedrock (1800 m below sea level, Fig. 1a). Effective pressure in this region is close to zero as high water pressure compensates for large ice overburden pressure. Similarly, the thick ice (2500 m, Fig. 1c) lying in a bed 1000–2000 m below sea level (Fig. 1a) in the main trunk results in high water pressure (Fig. 2a) and low effective pressure (Fig. 2c). Channelized drainage (Fig. 2c) is generated due to high water pressures (Fig. 2a), deep bedrock (Fig. 1a), and high basal melt (Fig. 1e).

Effective pressures are below 1 MPa in the main trunk, its large tributaries, and beneath the very thick ice in the south, leading to nonzero water sheet (Fig. 2d). Sheet thickness is relatively uniform ~0.2 m (Fig. 2d) and sheet discharge ~0.003 m^3 s^{-1} (Fig. 2b) in these regions suggesting an inefficient drainage system of poorly connected water pockets. As the ice accelerates towards the terminus (Fig. 1g), the increased melt rate (Fig. 1e) generates a sheet up to about 0.8 m thick near the start of the channels.

In the control experiment, channelized flow dominates the entire PIG domain as shown in Fig. 2. A well-established channel 130 km long is located at the central trough with uniform channel area of 500 m^2, equivalent to a cross-sectional diameter of 26 m. The discharge from the channelized system across the PIG grounding line is 51 m^3 s^{-1} (1.2 km^3 a^{-1}) with only another 0.09 m^2 s^{-1} from the distributed system. We also find a wide region with 0.8 m water depth, perhaps a "swamp" considering the likely presence of a few metres of sediment below the ice (Brisbourne et al., 2017), where water transforms from a distributed system into channelized system (Fig. 2d).

4.2. Sensitivity tests

We test the sensitivity of the basal hydrology system to different values of parameters in the model. We performed experiments using 38 combinations of parameters (Table 2). We compare the steady state outputs from all model runs with the base parameter set which we denote k_{s3}, k_{c2}, Ct_1 (Table 2).

Figs. 3 and 4 show the experiments using the channel conductivity of k_{c4} with different values of sheet conductivity. For a fixed channel conductivity, water drains less efficiently with lower sheet conductivity, leading to thicker water sheets, larger sheet area and more accumulation of water in the trunk. The modelled sheet thickness is <0.1 m when sheet conductivity is >0.01 m s kg^{-1} (i.e., k_{s1}, k_{s2}). However, the sheet thickness increases to 0.8 m with sheet conductivity <0.01 $m^{7/4}$ $kg^{-1/2}$ (i.e. k_{s3}, k_{s4}). The maximum depth of water sheet thickness is 0.8 m with the lowest sheet conductivity k_{s5} (Fig. 3e). A distributed drainage system is simulated in the fast flow region and southern PIG, consistent with low effective pressure in this area causing water accumulation.

Water sheet thickness over 0.7 m can be found along the central trunk in the experiments using the smallest channel conductivity k_{c4} (Fig. 3). In contrast, sheet thickness over the whole region is <0.3 m in the experiments using the largest channel conductivity, k_{c1} of 0.1 $m^{2/3}kg^{-1/2}$ (Fig. 4). The main difference in the modelled variables using different channel conductivity is the distribution of thick water sheet. The pattern of thin water layer is unaffected by changing channel conductivity values (Figs. 3 and 4).

Figs. 5, 6 & 7 show experiments with a fixed sheet conductivity of k_{s4} and k_{s3} and with different channel conductivity values. Sheet conductivity impacts the effective pressure distribution as the smaller sheet conductivity causes smaller effective pressure in the whole region. Effective pressure is slightly above 0 MPa in the fast-flowing region where most of the channels are located. As expected, water runs more efficiently using larger channel conductivity values with more arborescent channelization. We list the cross-sectional channel area and length using different channel conductivity values in Table 3. The main channel extends 139 km and 146 km upstream from the grounding line using k_{c1} and k_{c2}, but only 70 km and 43 km using k_{c3} and k_{c4}. The relation between the channel length and the channel conductivity value is not simply linear (Fig. 5; Table 3).

As channel conductivity is lowered, the channels become more concentrated near the grounding line and become shorter. The channel cross-sectional area shrinks as channel conductivities increase, as expected. Multiple channel tributaries are developed when channel

Table 2
Parameters values used in sensitivity experiments.

Description	Variable	Option	Value	Unit	Remark
Sheet conductivity	k_s	k_{s1}	10^{-1}	$m^{7/4}kg^{-1/2}$	Control
		k_{s2}	10^{-2}		
		k_{s3}	10^{-3}		
		k_{s4}	10^{-4}		
		k_{s5}	10^{-5}		
Channel conductivity	k_c	k_{c1}	10^{-1}	$m^{2/3}kg^{-1/2}$	Control
		k_{c2}	10^{-2}		
		k_{c3}	10^{-3}		
		k_{c4}	10^{-4}		
Pressure melt coefficient	c_t	C_{t1}	7.5×10^{-8}	KPa^{-1}	Control
		C_{t2}	0		

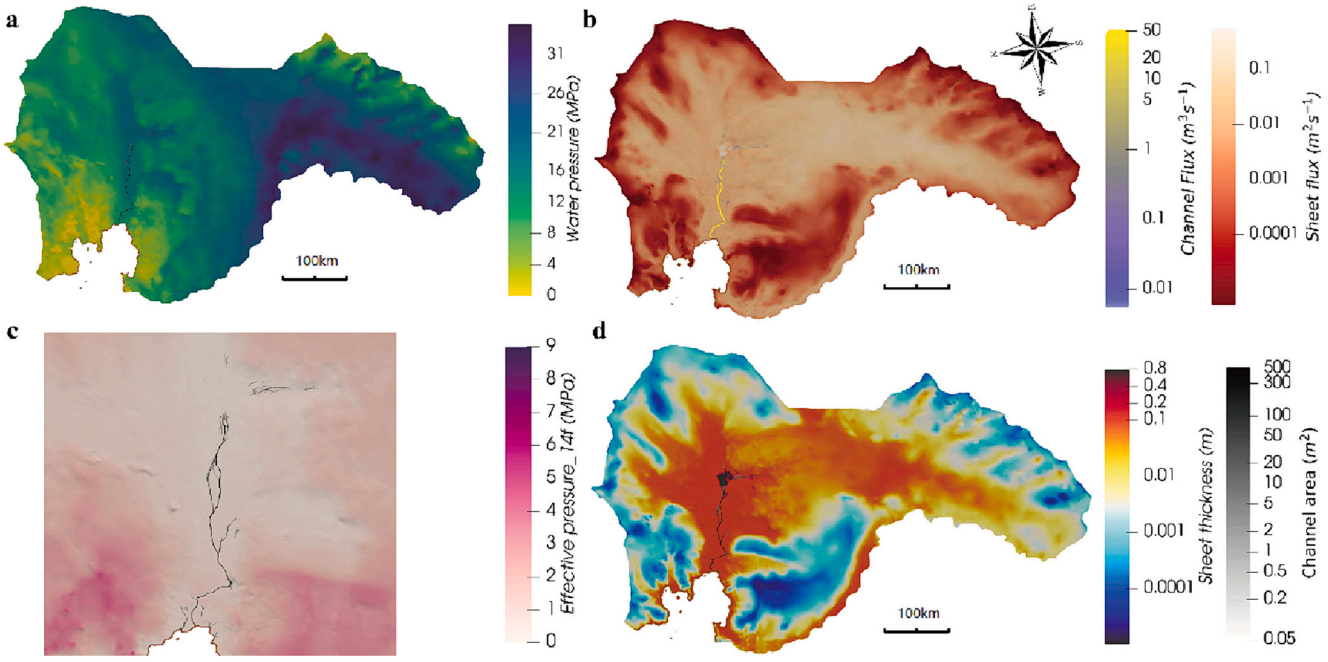

Fig. 2. Basal hydrology distribution from control run (parameters listed in Table 1). (a) water pressure (MPa); (b) sheet flux ($m^2\ s^{-1}$) in brown-orange shades with channel flux in colored curves ($m^3 s^{-1}$); (c) effective pressure (MPa) in zoomed-in region; (d) channel cross-sectional area (m^2) and water sheet thickness (m). Solid brown line shows the grounding line in all panels.

conductivity take the value of k_{c1} and k_{c2}.

Using the largest channel conductivity k_{c1}, multiple channels and more tributaries occur upstream when the sheet conductivity value is taken as $k_{s4} = 10^{-4}\ m^{7/4}\ kg^{-1/2}$, but only one tributary can be found when the sheet conductivity value is increased to $k_{s3} = 10^{-3}\ m^{7/4}\ kg^{-1/2}$ (Figs. 5a, 6a). The modelled channels using sheet conductivity value of k_{s3} are more concentrated (Fig. 6) than the arborescent pattern seen using the lowest sheet conductivity of k_{s4} (Fig. 5). The morphology of channels is sensitive to both channel conductivity and sheet conductivity.

We did experiments with different values of pressure melt coefficients, classical non-zero value c_{t1} and zero value c_{t2}. The dependency of melting point on pressure means that melt occurs more rapidly under pressure, increasing the channel opening rate (Eq. (12)). The pressure melt coefficient, c_t, has little influence on sheet system distribution, but does impact the pattern of channels, especially when channel conductivity is larger than $10^{-2}\ m^{2/3}kg^{-1/2}$ (Figs. 6a, 7a). The kink in the main channel (the same as in our control run in Figs. 2c, 3e) is retained when channel conductivity takes the large values of k_{c1} and k_{c2} if the melting-point is not dependent on pressure (Fig. 7a–b), but disappears and is replaced with an individual tributary of channel cross-sectional area = 1 m^2 when using pressure dependent melting point (Fig. 6a–b). This kink remains with the smaller channel conductivity values of k_{c3} and k_{c4} whether the pressure melting coefficient is c_{t1} or c_{t2}. Without considering the dependence of melting point on pressure, fewer tributaries occur along the central truck (Fig. 7a–b), especially for experiments using the large channel conductivity values of k_{c1} and k_{c2}. There are two segments of channels in eastern PIG when considering the pressure dependence of melting point (Fig. 6a–b), but they disappear without considering the dependence of melting point on pressure (Fig. 7a–b). The kink occurs in the southern side of the main trunk lies in the retrograde slope.

4.3. Spatial statistical analysis

To give an overview of all experiments conducted here and to analyze how spatial hydrology distribution is influenced by parameter choice, we examine the variability of the hydrological variables as a function of glacier flow speed (Figs. 8, 9). Basal sliding affects cavity opening rates in linked cavity systems (Kamb, 1987) leading to diversity in the basal hydrology system. We divide the whole domain into four ice flow regions and calculate the means of water layer thickness, water pressure and effective pressure in each region. Ice speeds over 300 m a^{-1} are defined as fast flow, medium ice speeds are between 100 and 300 m a^{-1}, slow speeds are from 10 to 100 m a^{-1}, and ice speeds below 10 m a^{-1} are super slow flow regions.

For $k_s \geqq 10^{-2}\ m^{7/4}\ kg^{-1/2}$, water layer thickness is <0.1 m (Fig. 8). Sheet conductivity $k_s = 10^{-2}\ m^{7/4}\ kg^{-1/2}$ marks a threshold above which sheet thickness and effective pressure as well as water pressure is largely unaffected by changing channel conductivity values. Water layer thickness slightly decreases when using larger sheet conductivity values.

For $k_s \leqq 10^{-3}\ m^{7/4}\ kg^{-1/2}$, water sheet thickness decreases as sheet conductivity rises (Fig. 8). The largest mean sheet thickness occurs in the fast flow region where it is 1.6 m when $k_s = 10^{-4}\ m^{7/4}\ kg^{-1/2}$ and is 0.52 m when $k_c = 10^{-3}\ m^{2/3}kg^{-1/2}$. The mean water sheet thickness is greater in the fast flow region (Fig. 8) than slower flow regions for most parameter choices because faster sliding means more frictional heating and higher melt rates. But there are some exceptions ($k_s = 10^{-4}\ m^{7/4}\ kg^{-1/2}$, $k_c = 10^{-1}$, $10^{-2}\ m^{2/3}\ kg^{-1/2}$) where thicker water sheets exist in the medium speed regions close to fast flow regions. The sheet thickness increases supra-linearly with k_c as k_s decreases from $10^{-3}\ m^{7/4}\ kg^{-1/2}$ to $10^{-4}\ m^{7/4}\ kg^{-1/2}$ in every flow region.

As sheet conductivity rises, water pressure falls and effective pressure (Fig. 9) rises. Lower channel conductivity leads to lower regional mean values of effective pressure. The relationship between ice flow and the regional mean of effective pressure is approximately linear, where faster ice flow causing lower effective pressure. The largest effective pressure of 7 MPa occur when k_s is largest through all experiments of $10^{-1}\ m^{7/4}\ kg^{-1/2}$ with all channel conductivity choices indicating the dominant distributed sheet system. This corresponds to the one of the smallest water pressure of 8 MPa occur at same parameter choice. Effective pressures are lowest in the fast flow region in all sensitivity tests (Fig. 9). When k_s is $10^{-3}\ m^{7/4}\ kg^{-1/2}$, water pressures exceed 52 % of ice overburden pressure (13 MPa) in the super slow region due to the

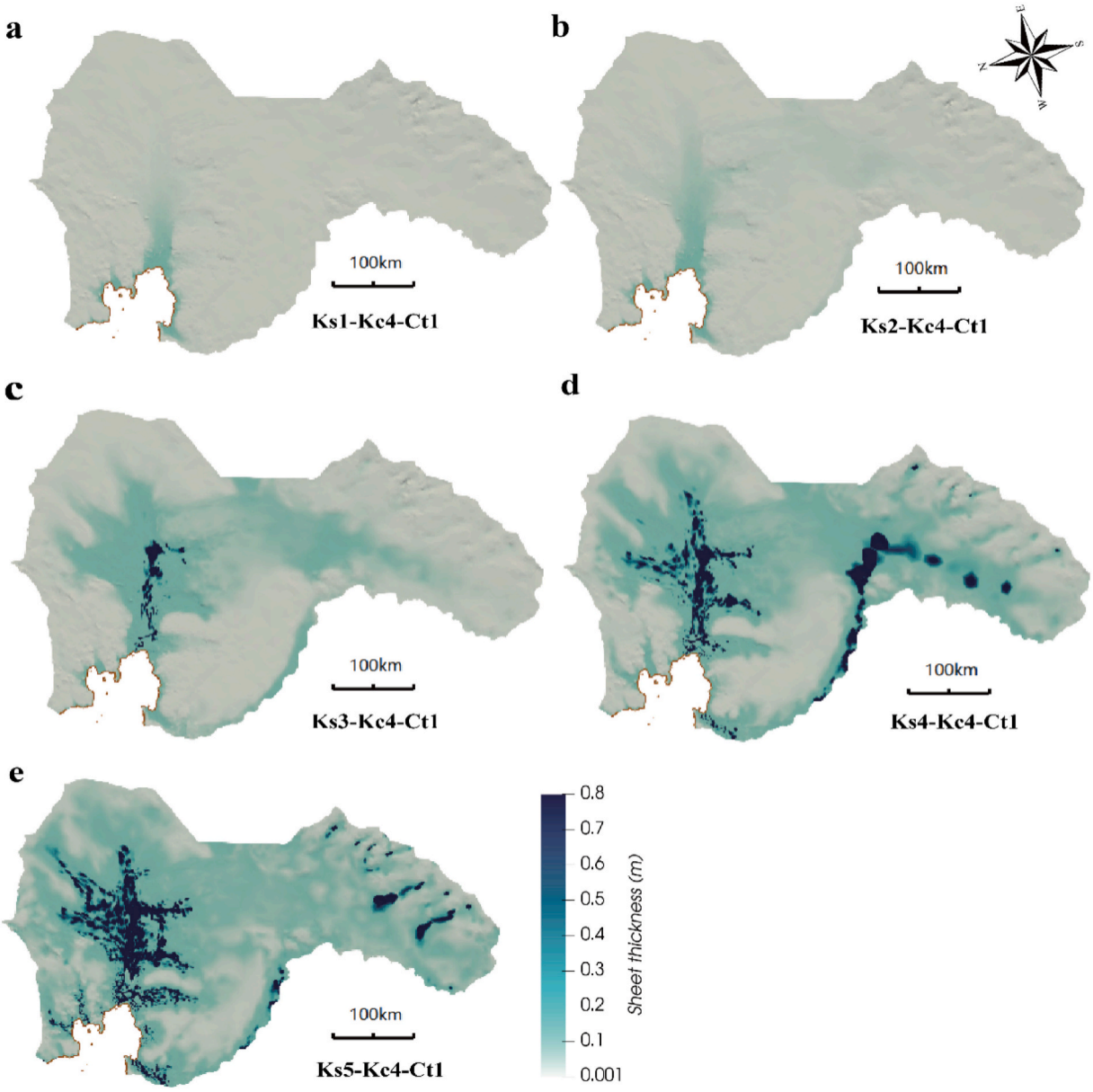

Fig. 3. Sheet thickness distribution with channel conductivity $k_{c4} = 10^{-4}$ $m^{2/3}$ $kg^{-1/2}$, $c_{t1} = 7.5 \times 10^{-8}$ K Pa^{-1} and different sheet conductivity values: (a) $k_{s1} = 10^{-1}$ $m^{7/4}$ $kg^{-1/2}$; (b) $k_{s2} = 10^{-2}$ $m^{7/4}$ $kg^{-1/2}$; (c) $k_{s3} = 10^{-3}$ $m^{7/4}$ $kg^{-1/2}$; (d) $k_{s4} = 10^{-4}$ $m^{7/4}$ $kg^{-1/2}$; (e) $k_{s5} = 10^{-5}$ $m^{7/4}$ $kg^{-1/2}$. The brown curve is the grounding line.

extremely high ice overburden pressure.

Results from our statistical analysis are consistent with the description of experiments in Section 4.2, larger sheet conductivity values cause water flow to be organized into a channelized system with higher water pressure and a thinner water layer. Sheet conductivity is the dominant control on basal conditions especially in the fast-flowing region. When $k_s \geqq 10^{-3}$ $m^{7/4}$ $kg^{-1/2}$, channel conductivity barely influences basal discharge and the distribution of the hydrology system.

5. Discussion

5.1. Channelization on Pine Island Glacier

In our control experiment with "standard parameters", we found a stable state with a 130 km subglacial channel with 500 m^2 cross-sectional area had evolved after 145 years of simulation beneath Pine Island Glacier. Channelized discharge dominated in the PIG central trough with relatively low water pressure and low effective pressure. Channel discharge was 51 m^3 s^{-1} across the Pine Island Glacier grounding line. This is close to the discharge volume estimated by Joughin et al. (2009) of 53 m^3 s^{-1} from purely ice dynamic modelling.

About the same discharge, 42 m^3 s^{-1} was hydrologically modelled for Totten Glacier (Dow et al., 2020) with similar magnitude of basal water production rates and a somewhat larger, 80 m^3 s^{-1}, discharge for Thwaites Glacier (Hager et al., 2022). Channel lengths of 50–100 km and 100–200 km were simulated for these two glaciers respectively.

In theory, subglacial channels are not expected to develop when distributed discharge is lower than some critical discharge, especially with negligible surface water input to the basal hydrologic system as in Antarctica (Hewitt, 2011; Schoof, 2010). However, we find stable subglacial channels for most parameter choices, except in some large basal conductivity situations. These channels are favored by several factors: 1) relatively high basal melt rates of 1 m a^{-1} generated by frictional heating when sliding over of sticky spots near the terminus; 2) a central trough bed geometry; 3) large catchment size generating enough water to accumulate in the trough and form stable channelized drainage.

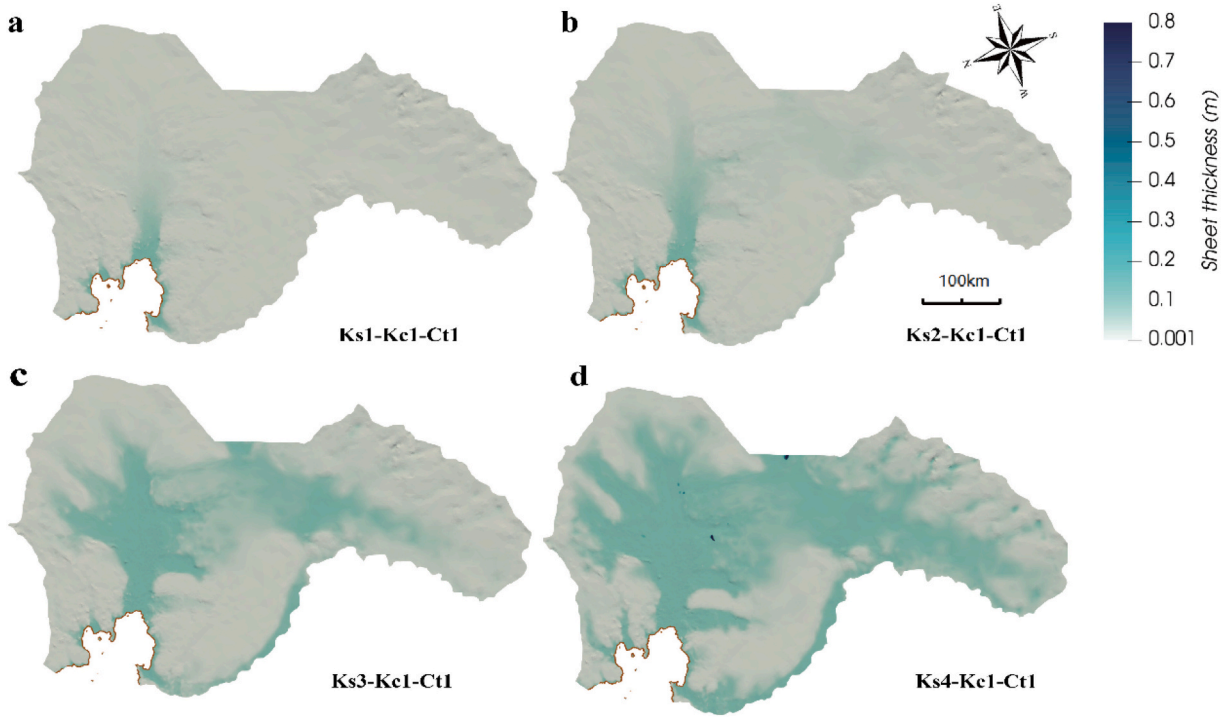

Fig. 4. Sheet thickness distribution with channel conductivity $k_{c1} = 10^{-1}$ $m^{2/3}kg^{-1/2}$, $c_{t1} = 7.5 \times 10^{-8}$ K Pa^{-1} and different sheet conductivity values: (a) $k_{s1} = 10^{-1}$ $m^{7/4}$ $kg^{-1/2}$; (b) $k_{s2} = 10^{-2}$ $m^{7/4}$ $kg^{-1/2}$; (c) $k_{s3} = 10^{-3}$ $m^{7/4}$ $kg^{-1/2}$; (d) $k_{s4} = 10^{-4}$ $m^{7/4}$ $kg^{-1/2}$. The brown curve is the grounding line.

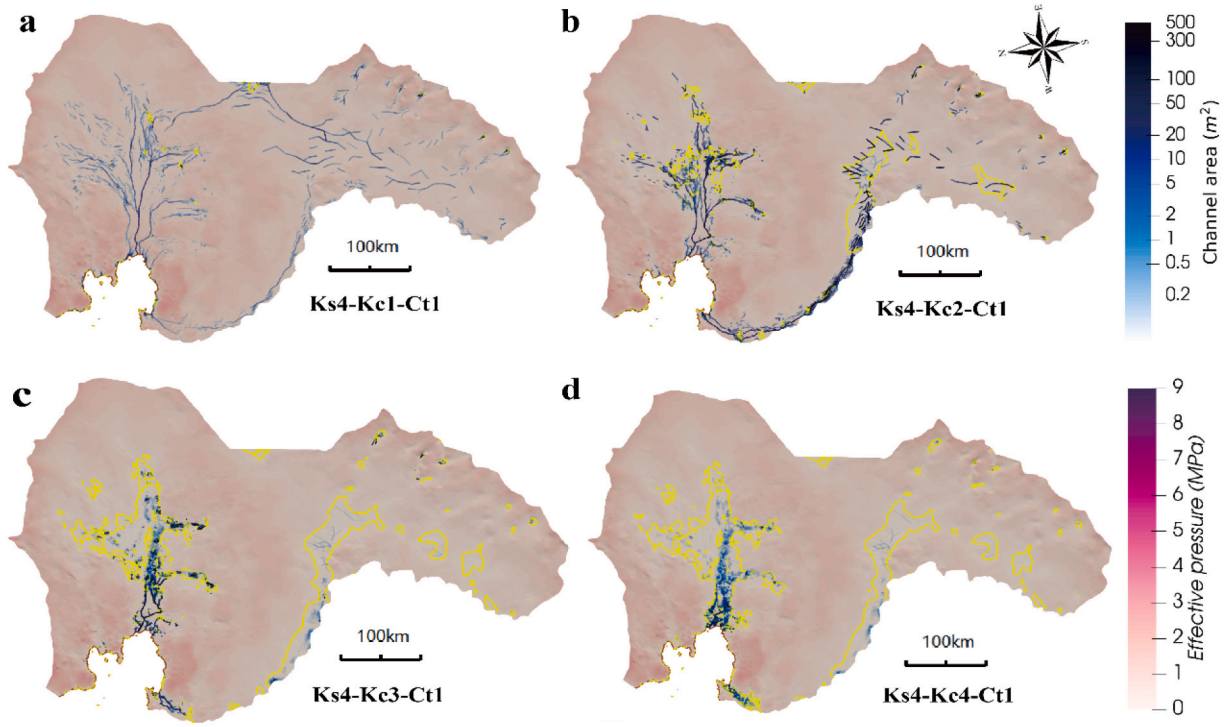

Fig. 5. Effective pressure distribution and channel area with sheet conductivity $k_{s4} = m^{7/4}$ $kg^{-1/2}$, $c_{t1} = 7.5 \times 10^{-8}$ K Pa^{-1} and different channel conductivity values; (a) $k_{c1} = 10^{-1}$ $m^{2/3}kg^{-1/2}$; (b), $k_{c2} = 10^{-2}$ $m^{2/3}kg^{-1/2}$; (c) $k_{c3} = 10^{-3}$ $m^{2/3}kg^{-1/2}$; (d) $k_{c4} = 10^{-4}$ $m^{2/3}kg^{-1/2}$. The brown curve is the grounding line. The yellow curve is the contour of 0.15 MPa effective pressure.

We adopted a wide range of parameter choices for basal conductivities and examined the pressure-dependency to explore how the efficient drainage system functions and its stability in our simulation. Not all parameter choices give the well-established channels as in our control run. Channels are barely established with sheet conductivities larger than 10^{-2} $m^{7/4}$ $kg^{-1/2}$ while channel conductivities are larger than 10^{-3} $m^{2/3}$ $kg^{-1/2}$. This is consistent with some other sensitivity tests (Werder et al., 2013) of testing GlaDS on synthetic topographies where larger

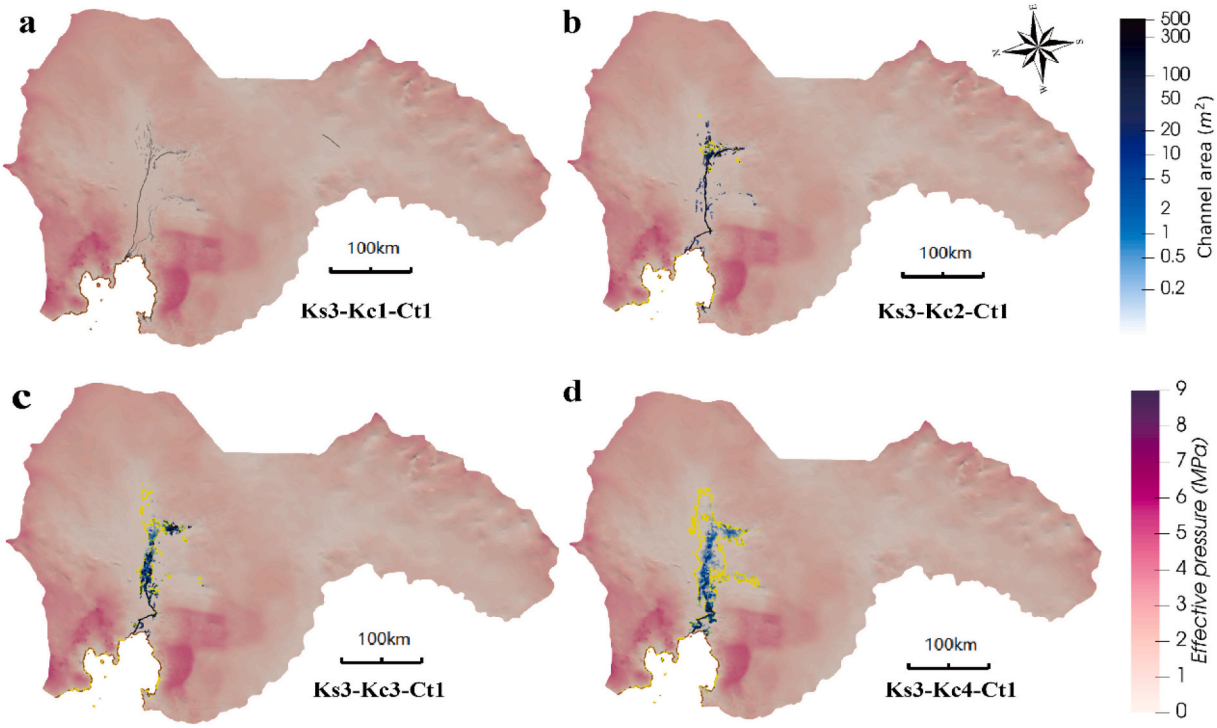

Fig. 6. Effective pressure distribution and channel area with sheet conductivity $k_{s3} = 10^{-3}\ m^{7/4}\ kg^{-1/2}$, $c_{t1} = 7.5 \times 10^{-8}\ K\ Pa^{-1}$ and different channel conductivity values: (a) $k_{c1} = 10^{-1}\ m^{2/3}kg^{-1/2}$; (b), $k_{c2} = 10^{-2}\ m^{2/3}kg^{-1/2}$; (c) $k_{c3} = 10^{-3}\ m^{2/3}kg^{-1/2}$; (d) $k_{c4} = 10^{-4}\ m^{2/3}kg^{-1/2}$. The brown curve is the grounding line. The yellow curve is the contour of 0.15 MPa effective pressure.

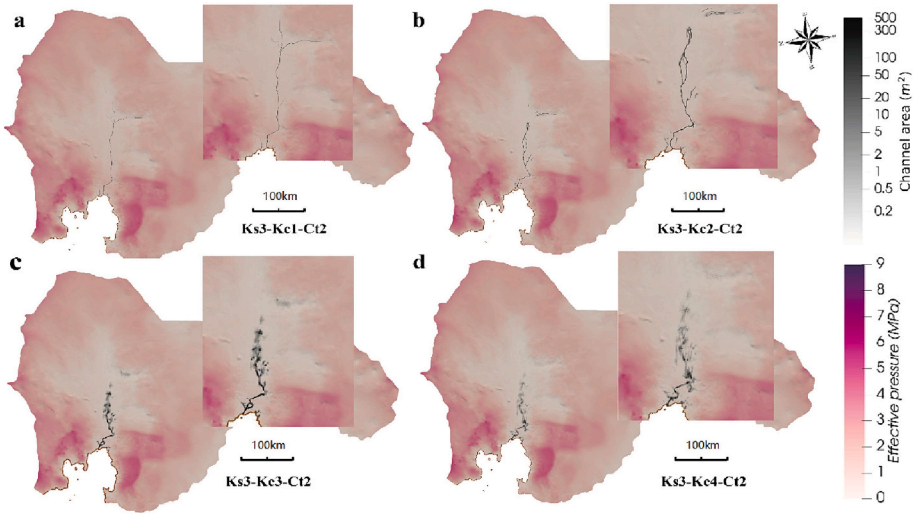

Fig. 7. Effective pressure distribution and channel area with sheet conductivity $k_{s3} = 10^{-3}\ m^{7/4}\ kg^{-1/2}$, $c_{t2} = 0\ K\ Pa^{-1}$ and different channel conductivity values: (a) $k_{c1} = 10^{-1}\ m^{2/3}kg^{-1/2}$; (b) $k_{c2} = 10^{-2}\ m^{2/3}kg^{-1/2}$; (c) $k_{c3} = 10^{-3}\ m^{2/3}kg^{-1/2}$; (d) $k_{c4} = 10^{-4}\ m^{2/3}kg^{-1/2}$. The brown curve is the grounding line. Enlargements of channelized region are shown in the insets.

Table 3
Channel characteristic with fixed sheet conductivity value $k_{s3} = 10^{-3}\ m^{7/4}\ kg^{-1/2}$.

Channel conductivity identification	Channel conductivity ($m^{2/3}kg^{-1/2}$)	Channel cross-sectional area near grounding line (m^2)	Channel extension length (km)
k_{c1}	10^{-1}	25	139
k_{c2}	10^{-2}	300	146
k_{c3}	10^{-3}	500	70
k_{c4}	10^{-4}	500	43

basal conductivity values cause barely any channels to form. The real-world topographies in the refined meshes we use in fast flowing channelized drainage region increase the credibility of the channelized simulations. The detailed results also capture branches and tributaries with much smaller cross-sectional area.

5.2. Model considerations on Pine Island Glacier

Since there is no direct observational data on basal material conductivity, or basal sliding speed as well as water production beneath Pine Island Glacier and hence no empirical evidence of the basal

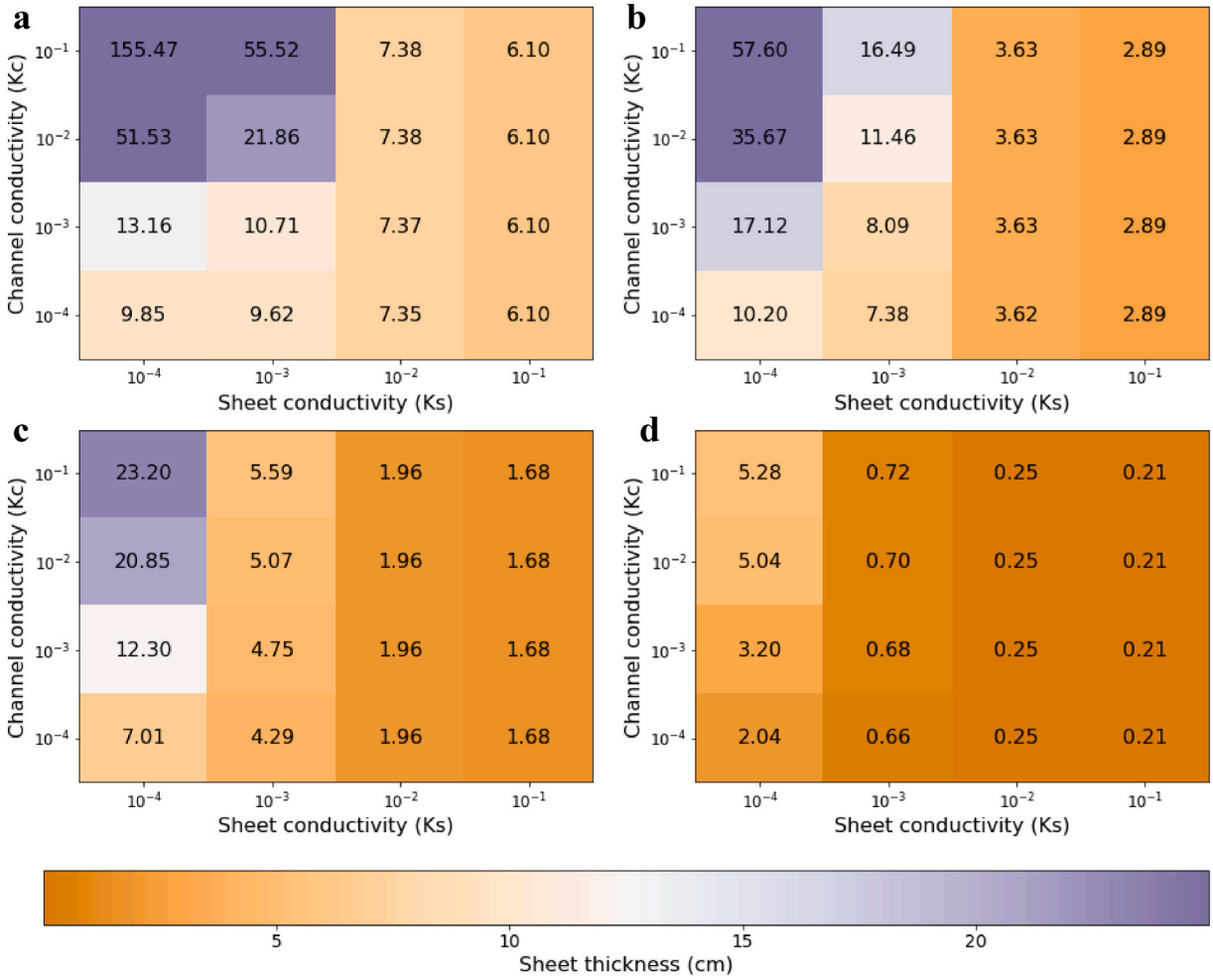

Fig. 8. Spatial analysis of hydrologic conductivities: discrete heat map of area mean of sheet thickness (cm) in (a) fast-flowing area; (b) medium-flowing area; (c) slow-flowing area; (d) super slow-flowing area.

conductivities that might be appropriate, we use spatially and temporally uniform water sheet and channel conductivity values similar as used in synthetic Greenland-like settings (Gagliardini and Werder, 2018; Werder et al., 2013), and applied to Totten Glacier (Dow et al., 2020) in Antarctica. The basal sliding speed and basal melt from the ice dynamics inversion in Elmer/Ice are spatially variable but since they are steady state, they cannot evolve over time in response to the evolving basal hydrology. There is a possible problem that hard-bed sheet conductivity values may not be appropriate for a system with plenty of soft sediments in reality (Joughin et al., 2009; Brisbourne et al., 2017).

The PIG grounding line retreated 31 km along its center line from 1992 to 2001 (Rignot et al., 2014). In our model setup, a fixed grounding line was adopted because of limitations in computing time needed to run a time-evolving ice sheet model, and the difficulties in setting up the initial state that matches observations. Consideration of transient grounding line motion is a desirable feature for realistic future simulation of the glacier, but providing a suitable starting condition is challenging.

5.3. Impact on ice dynamics

Although there is feedback between ice dynamics and basal hydrology, and thus, arguably, the hydrologic system may never reach a steady state. Therefore, one may ask, is our steady-state analysis useful for understanding the current state of PIG? This question can be affirmed with the following argument: The time the simulation needs to reach steady state (about 150 years) shows that the hydrologic system is likely close to a steady state as the ice dynamics and geometry PIG was relatively stable over the past 150 years. So, our results should reproduce the current state closely. Of course, for a simulation of the future evolution of PIG, the steady state assumption may well break down with the likely rapid changes in geometry and possible future water input from surface melt. Thus, this study lays the groundwork for such future works by providing plausible initial conditions for projective simulations.

Ice dynamic models are used to evaluate glacier mass loss (Shepherd et al., 2018) and project their contribution to sea level rise by assessing ice sheet retreat, bedrock uplift and other effects that impact sea level rise (Gomez et al., 2015; Seroussi et al., 2020). The full set of physical processes forming the coupled ice dynamic – hydrologic system, which exert significant control over ice sliding speeds, have not been included in model based projections of the Antarctic Ice Sheet; instead basal friction parameterizations are used to aggregate the subglacial hydrology conditions. Our simulations show that the presence of basal meltwater, and its discharge through the distributed sheet system, leads to increased basal water pressures compared to the commonly used assumption of full connectivity to the ocean in which effective pressure is determined by height above floatation. Conversely, the presence of channelization in the central trough can efficiently discharge basal water, reducing basal water pressures. The net effect is, in all of our simulations, an effective pressure distribution that is lower everywhere than would be implied by the ocean connectivity assumption. In the time evolving coupled system the competing effects of efficient channelized

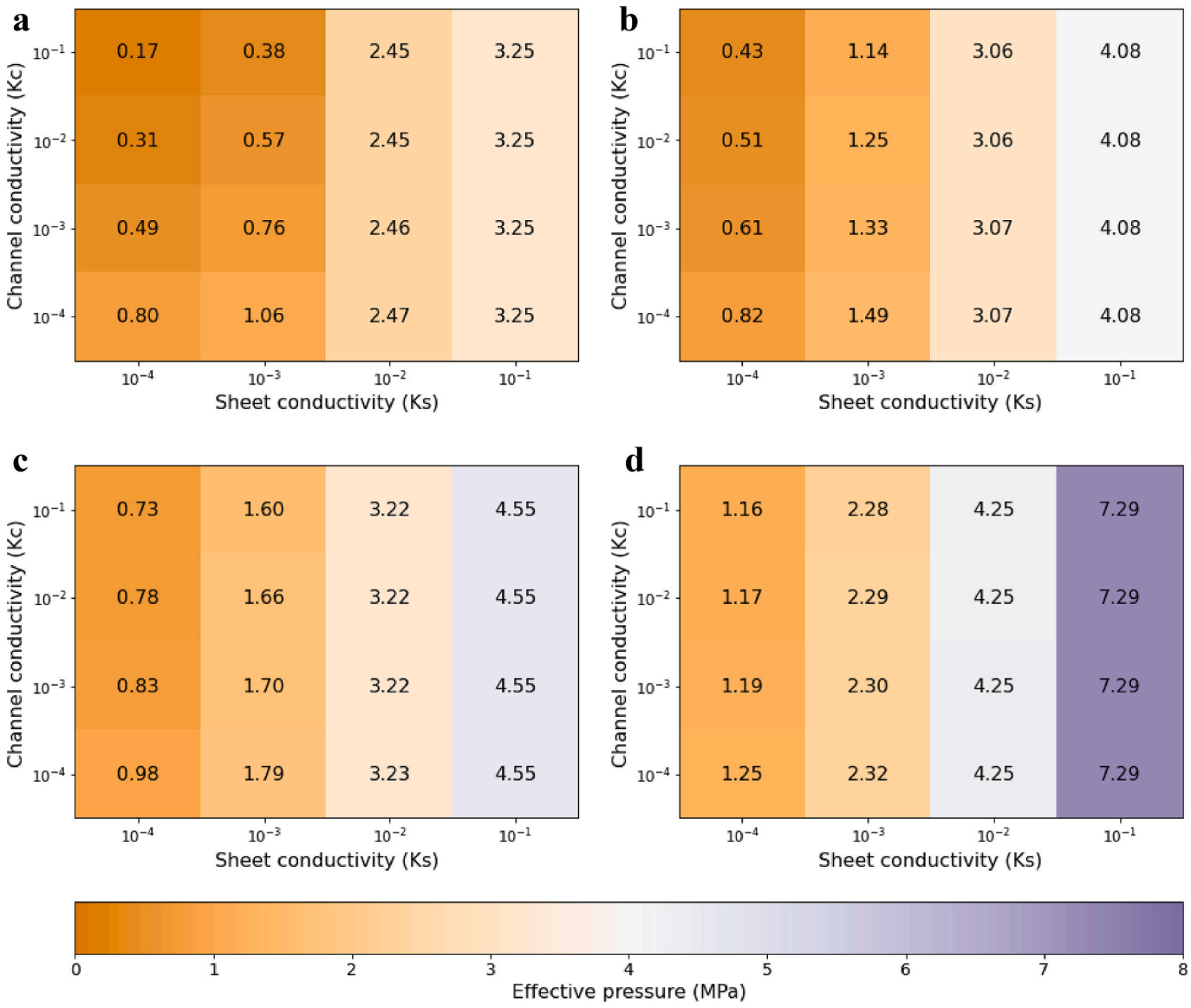

Fig. 9. Spatial analysis of hydrologic conductivities: discrete heat map of area mean of effective pressure (MPa) in (a) fast-flowing area; (b) medium-flowing area; (c) slow-flowing area; (d) super slow-flowing area.

drainage and less efficient distributed drainage are likely to compete to determine whether the subglacial feedback on ice dynamics is likely to be positive or negative in steady state. However, the immediate response is likely to be positive: increased sliding leads to increased melting, more water in the hydrologic system, and therefore higher water pressures, allowing faster sliding and increased friction heat providing more melt water (Hoffman and Price, 2014). Whether the steady state of the perturbed coupled system, to which the system evolves towards, has increased or decreased ice flow speeds, would need to be investigated with a fully coupled model.

The presence of a channelized subglacial outlet at the grounding line promotes formation of a turbulent plume of low density water that entrains warmer and more saline ocean water as it rises along the floating parts of the glacier. This turbulent plume acts to increase basal melt rates that thin the floating ice shelf, reducing buttressing acting on the grounded glacier (Nakayama et al., 2021), potentially leading to a positive feedback as grounded acceleration increases friction heat and therefore also total grounded melt water produced.

5.4. Basal material

A thin (<10 m) sediment layer (Brisbourne et al., 2017) beneath the main trunk of PIG with underlying igneous rock is inferred from seismic and airborne-gravity data 20 km upstream from the grounding line (Smith et al., 2012), with erosion rates of 1 m a^{-1}. The distribution of the deformable sediment layer has not been well constrained by the so-far limited seismic profiles (Brisbourne et al., 2017). However, GlaDS is constructed assuming water flows at hard bedrock with weak hydraulic conductivity. Weak hydraulic conductivity represents poorly connected regions of the system (when $k_s \leqq 10^{-3}$ $m^{2/3}$ $kg^{-1/2}$) and high basal conductivity approximately represents the presence of sediments ($k_s > 10^{-3}$ $m^{2/3}$ $kg^{-1/2}$). We explored a wide range of channel and sheet parameter choices over four orders of magnitude to represent basal material hydrological properties (Section 4.2). The well-organized channelized hydrology system beneath Pine Island Glacier exists when we used relatively weak connectivity ($k_s = 10^{-3}$ $m^{2/3}$ $kg^{-1/2}$) in our control experiment. The likely presence of sediment ($k_s > 10^{-3}$ $m^{2/3}$ $kg^{-1/2}$) can cause the channel conductivity to become ineffective. Basal material impacts the basal drainage system since water can penetrate

into the till layer, which may then deform rather than the sliding taking place purely at the base of the ice, and till permeability affects water accumulation in the drainage system (Bingham et al., 2017).

6. Conclusion

We applied the parallel implementation of GlaDS model, which incorporates both distributed and channelized system components, to simulate the basal hydrologic system beneath Pine Island Glacier. We used inputs inferred through optimization of a full-Stokes flow ice dynamic model to match observed surface velocities. A wide range of parameters were employed to study a range of plausible hydrology distributions beneath Pine Island Glacier.

Key results from our study include the likely presence of stable channels under the glacier extending 100–200 km inland along the central trunk due to the meltwater production over most of the PIG catchment being routed along the PIG central trunk. During model spin-up, channels begin to form in sections, especially close to the grounding line, and become linked as the simulation approaches steady state. The presence and extent of channels in the steady state system depends on the relative conductivities defined in the distributed sheet system and in the channelized system, with high channel conductivity and low sheet conductivity leading to the most extensive channelization.

Relatively high water pressures build up to 84 % of ice overburden pressure in the central trunk of Pine Island Glacier where ice velocities are very high and the hydraulic potential gradient is low. Water pressure approaches ice overburden pressure, causing very low effective pressure in the region, facilitating fast glacier sliding. Parameter choices influence our drainage morphology, especially the channelized flow, with a threshold behavior in terms of sheet conductivity: when sheet conductivity is above $10^{-2}\,m^{7/4}\,kg^{-1/2}$, choice of channel conductivity does not significantly impact the hydrology system (more specifically, sheet thickness and effective pressure are not sensitive to channel conductivity in this regime). In this sheet dominated regime we anticipate a positive feedback between glacier sliding and the hydrologic system: faster sliding leads to more friction heat, more water in the hydrologic system, higher water pressures and therefore faster sliding. However, when the sheet system becomes overloaded the excess water pressure may cause opening of efficient drainage channels, allowing a more rapid discharge of basal water and potentially even reversing the sign of the feedback. Simulation with a coupled hydrology-ice dynamics system would be needed to verify these anticipated feedbacks.

Given this threshold behavior in the channelized vs distributed sheet system and its sensitivity to sheet conductivity, these relative conductivities may determine not only the strength of a potential feedback between the ice dynamic regime and the hydrologic system, but also even the sign of the feedback.

Given these findings, we suggest that an improved understanding of the net conductivity through the distributed sheet system (including impacts of sediment hydrology), and model coupling between ice dynamics and subglacial hydrologic system, are likely the most crucial developments needed to improve model-based predictive capability for the Pine Island Glacier and, more generally, the Antarctic Ice Sheet.

Supplementary data to this article can be found online at https://doi.org/10.1016/j.scitotenv.2024.172144.

CRediT authorship contribution statement

Yufang Zhang: Writing – review & editing, Writing – original draft, Methodology, Formal analysis. **John C. Moore:** Writing – review & editing, Project administration, Funding acquisition, Conceptualization. **Liyun Zhao:** Writing – review & editing, Funding acquisition. **Mauro A. Werder:** Writing – review & editing, Methodology, Formal analysis. **Rupert Gladstone:** Data curation, Funding acquisition, Methodology. **Michael Wolovick:** Writing – review & editing, Data curation, Conceptualization.

Declaration of competing interest

The authors declare that they have no known competing financial interests or personal relationships that could have appeared to influence the work reported in this paper.

Data availability

Data will be made available on request.

Acknowledgments

This work was supported by National Key Research and Development Program of China (grant no. 2021YFB3900105) and Finnish Academy COLD Consortium (grant no. 322430 and 322978). The author is also founded by China Scholarship Council for research collaboration.

References

Andrews, L.C., Catania, G.A., Hoffman, M.J., Gulley, J.D., Lüthi, M.P., Ryser, C., Hawley, R.L., Neumann, T.A., 2014 Oct 2. Direct observations of evolving subglacial drainage beneath the Greenland Ice Sheet. Nature 514 (7520), 80–83. https://doi.org/10.1038/nature13796.

Beyer, S., Kleiner, T., Aizinger, V., Rückamp, M., Humbert, A., 2018. A confined-unconfined aquifer model for subglacial hydrology and its application to the Northeast Greenland Ice Stream. Cryosphere 12, 3931–3947. https://doi.org/10.5194/TC-12-3931-2018.

Bingham, R.G., Vaughan, D.G., King, E.C., Davies, D., Cornford, S.L., Smith, A.M., Arthern, R.J., Brisbourne, A.M., De Rydt, J., Graham, A.G.C., Spagnolo, M., Marsh, O.J., Shean, D.E., 2017. Diverse landscapes beneath Pine Island Glacier influence ice flow. Nat. Commun. 8, 1–9. https://doi.org/10.1038/s41467-017-01597-y.

Brinkerhoff, D., Aschwanden, A., Fahnestock, M., 2021. Constraining subglacial processes from surface velocity observations using surrogate-based Bayesian inference. J. Glaciol. 67 (263), 385–403. https://doi.org/10.1017/jog.2020.112.

Brisbourne, A.M., Smith, A.M., Vaughan, D.G., King, E.C., Davies, D., Bingham, R.G., Smith, E.C., Nias, I.J., Rosier, S.H.R., 2017. Bed conditions of Pine Island Glacier, West Antarctica. Case Rep. Med. 122, 419–433. https://doi.org/10.1002/2016JF004033.

Chu, W., Schroeder, D.M., Seroussi, H., Creyts, T.T., Palmer, S.J., Bell, R.E., 2016. Extensive winter subglacial water storage beneath the Greenland Ice Sheet. Geophys. Res. Lett. 43 (12) https://doi.org/10.1002/2016GL071538 (484-12, 492).

Cowton, T., Nienow, Peter, Sole, Andrew, Wadham, Jemma, Lis, Greg, Bartholomew, Ian, Mair, Doug, Chandler, Dave, Nienow, P., Sole, A., Wadham, J., Lis, G., Bartholomew, I., Mair, D., Chandler, D., 2013. Evolution of drainage system morphology at a land-terminating Greenlandic outlet glacier. Case Rep. Med. 118, 29–41. https://doi.org/10.1029/2012JF002540.

De Fleurian, B., Werder, M.A., Beyer, S., Brinkerhoff, D.J., Delaney, I., Dow, C.F., Downs, J., Gagliardini, O., Hoffman, M.J., Hooke, R.L., Seguinot, J., Sommers, A.N., 2018. SHMIP the subglacial hydrology model intercomparison project. J. Glaciol. 64, 897–916. https://doi.org/10.1017/JOG.2018.78.

Dow, C.F., Karlsson, N.B., Werder, M.A., 2018a. Limited impact of subglacial supercooling freeze-on for Greenland ice sheet stratigraphy. Geophys. Res. Lett. 45 (3), 1481–1489. https://doi.org/10.1002/2017GL076251.

Dow, C.F., Werder, M.A., Babonis, G., et al., 2018b. Dynamics of active subglacial lakes in Recovery Ice Stream. J. Geophys. Res. Earth 123 (4), 837–850. https://doi.org/10.1002/2017JF004409.

Dow, C.F., McCormack, F.S., Young, D.A., Greenbaum, J.S., Roberts, J.L., Blankenship, D. D., 2020. Totten Glacier subglacial hydrology determined from geophysics and modeling. Earth Planet. Sci. Lett. 531, 115961 https://doi.org/10.1016/j.epsl.2019.115961.

Dow, C.F., Ross, N., Jeofry, H., Siu, K., Siegert, M.J., 2022. Antarctic basal environment shaped by high-pressure flow through a subglacial river system. Nat. Geosci. 15 https://doi.org/10.1038/s41561-022-01059-1.

Drews, R., Pattyn, F., Hewitt, I., et al., 2017. Actively evolving subglacial conduits and eskers initiate ice shelf channels at an Antarctic grounding line. Nat. Commun. 8, 15228 https://doi.org/10.1038/ncomms15228.

Flowers, G.E., Björnsson, H., Pálsson, F., Clarke, G.K.C., 2004. A coupled sheet-conduit mechanism for jökulhlaup propagation. Geophys. Res. Lett. https://doi.org/10.1029/2003gl019088.

Gagliardini, O., Werder, M.A., 2018. Influence of increasing surface melt over decadal timescales on land-terminating Greenland-type outlet glaciers. J. Glaciol. 64, 700–710. https://doi.org/10.1017/jog.2018.59.

Gladstone, R., Wang, Y., 2022. Antarctic Regional Inversions Using Elmer/Ice: Methodology. Zenodo. https://doi.org/10.5281/zenodo.5862046.

Gladstone, R., Schäfer, M., Zwinger, T., Gong, Y., Strozzi, T., Mottram, R., Boberg, F., Moore, J.C., 2014. Importance of basal processes in simulations of a surging Svalbard outlet glacier. Cryosphere 8, 1393–1405. https://doi.org/10.5194/tc-8-1393-2014.

Gomez, N., Pollard, D., Holland, D., 2015. Sea-level feedback lowers projections of future Antarctic Ice-Sheet mass loss. Nat. Commun. 6, 1–8. https://doi.org/10.1038/ncomms9798.

Hager, A.O., Hoffman, M.J., Price, S.F., Schroeder, D.M., 2022. Persistent, extensive channelized drainage modeled beneath Thwaites Glacier, West Antarctica. Cryosphere 16, 3575–3599. https://doi.org/10.5194/tc-16-3575-2022.

Hewitt, I.J., 2011. Modelling distributed and channelized subglacial drainage: the spacing of channels. J. Glaciol. 57, 302–314. https://doi.org/10.3189/002214311796405951.

Hoffman, M.J., Price, S., 2014. Feedbacks between coupled subglacial hydrology and glacier dynamics. Case Rep. Med. 119, 414–436. https://doi.org/10.1002/2013JF002943.

Huang, Y., Zhao, L., Wolovick, M., Ma, Y., Moore, J.C., 2024. Using specularity content to evaluate eight geothermal heat flow maps of Totten Glacier. Cryosphere 18, 103–119. https://doi.org/10.5194/tc-18-103-2024.

Joughin, I., Tulaczyk, S., Bamber, J.L., Blankenship, D., Holt, J.W., Scambos, T., Vaughan, D.G., 2009. Basal conditions for Pine Island and Thwaites Glaciers, West Antarctica, determined using satellite and airborne data. J. Glaciol. 55, 245–257. https://doi.org/10.3189/002214309788608705.

Joughin, I., Smith, B.E., Holland, D.M., 2010. Sensitivity of 21st century sea level to ocean-induced thinning of Pine Island Glacier, Antarctica. Geophys. Res. Lett. 37, 1–5. https://doi.org/10.1029/2010GL044819.

Kamb, B., 1987. Glacier surge mechanism based on linked cavity configuration of the basal water conduit. System 92, 9083–9100. https://doi.org/10.1029/JB092iB09p09083.

Le Brocq, A., Ross, N., Griggs, J., et al., 2013. Evidence from ice shelves for channelized meltwater flow beneath the Antarctic Ice Sheet. Nat. Geosci. 6, 945–948. https://doi.org/10.1038/ngeo1977.

Morlighem, M., Rignot, E., Binder, T., Blankenship, D., Drews, R., Eagles, G., Eisen, O., Ferraccioli, F., Forsberg, R., Fretwell, P., Goel, V., Greenbaum, J.S., Gudmundsson, H., Guo, J., Helm, V., Hofstede, C., Howat, I., Humbert, A., Jokat, W., Karlsson, N.B., Lee, W.S., Matsuoka, K., Millan, R., Mouginot, J., Paden, J., Pattyn, F., Roberts, J., Rosier, S., Ruppel, A., Seroussi, H., Smith, E.C., Steinhage, D., Sun, B., van den Broeke, M.R., van Ommen, T.D., van Wessem, M., Young, D.A., 2019. Deep glacial troughs and stabilizing ridges unveiled beneath the margins of the Antarctic ice sheet. Nat. Geosci. 13 (2), 132–137. https://doi.org/10.1038/s41561-019-0510-8.

Nakayama, Y., Cai, C., Seroussi, H., 2021. Impact of subglacial freshwater discharge on Pine Island Ice Shelf. Geophys. Res. Lett. 48 https://doi.org/10.1029/2021GL093923.

Nye, J.F., 1976. Water flow in glaciers: jökulhlaups, tunnels and veins. J. Glaciol. 17, 181–207. https://doi.org/10.3189/s002214300001354.

Rignot, E., Mouginot, J., Morlighem, M., Seroussi, H., Scheuchl, B., 2014. Widespread, rapid grounding line retreat of Pine Island, Thwaites, Smith, and Kohler glaciers, West Antarctica, from 1992 to 2011. Geophys. Res. Lett. 41, 3502–3509. https://doi.org/10.1002/2014GL060140.

Rignot, E., Mouginot, J., Scheuchl, B., Van Den Broeke, M., Van Wessem, M.J., Morlighem, M., 2019. Four decades of Antarctic ice sheet mass balance from 1979–2017. Proc. Natl. Acad. Sci. U. S. A. 116, 1095–1103. https://doi.org/10.1073/PNAS.1812883116.

Rignot, E., Mouginot, J., Scheuchl, B., Jeong, S., 2022. Changes in Antarctic ice sheet motion derived from satellite radar interferometry between 1995 and 2022. Geophys. Res. Lett. 49 https://doi.org/10.1029/2022GL100141.

Röthlisberger, H., 1972. Water pressure in subglacial channels. J. Glaciol. 2, 177–203. https://doi.org/10.3189/S0022143000022188.

Schoof, C., 2010. Ice-sheet acceleration driven by melt supply variability. Nature 468, 803–806. https://doi.org/10.1038/nature09618.

Schroeder, D.M., Blankenship, D.D., Young, D.A., 2013. Evidence for a water system transition beneath Thwaites Glacier, West Antarctica. Proc. Natl. Acad. Sci. U.S.A. 110, 12225–12228. https://doi.org/10.1073/pnas.1302828110.

Schroeder, D.M., Blankenship, D.D., Raney, R.K., Grima, C., 2015. Estimating subglacial water geometry using radar bed echo specularity: application to Thwaites Glacier, West Antarctica. IEEE Geosci. Remote Sens. Lett. 12, 443–447. https://doi.org/10.1109/LGRS.2014.2337878.

Seroussi, H., Nowicki, S., Payne, A.J., Goelzer, H., Lipscomb, W.H., Abe-Ouchi, A., Agosta, C., Albrecht, T., Asay-Davis, X., Barthel, A., Calov, R., Cullather, R., Dumas, C., Galton-Fenzi, B.K., Gladstone, R., Golledge, N.R., Gregory, J.M., Greve, R., Hattermann, T., Hoffman, M.J., Humbert, A., Huybrechts, P., Jourdain, N. C., Kleiner, T., Larour, E., Leguy, G.R., Lowry, D.P., Little, C.M., Morlighem, M., Pattyn, F., Pelle, T., Price, S.F., Quiquet, A., Reese, R., Schlegel, N.J., Shepherd, A., Simon, E., Smith, R.S., Straneo, F., Sun, S., Trusel, L.D., Van Breedam, J., Van De Wal, R.S.W., Winkelmann, R., Zhao, C., Zhang, T., Zwinger, T., 2020. ISMIP6 Antarctica: a multi-model ensemble of the Antarctic ice sheet evolution over the 21st century. Cryosphere 14, 3033–3070. https://doi.org/10.5194/tc-14-3033-2020.

Shepherd, A., Ivins, E., Rignot, E., Smith, B., Van Den Broeke, M., Velicogna, I., Whitehouse, P., Briggs, K., Joughin, I., Krinner, G., Nowicki, S., Payne, T., Scambos, T., Schlegel, N., Geruo, A., Agosta, C., Ahlstrøm, A., Babonis, G., Barletta, V., Blazquez, A., Bonin, J., Csatho, B., Cullather, R., Felikson, D., Fettweis, X., Forsberg, R., Gallee, H., Gardner, A., Gilbert, L., Groh, A., Gunter, B., Hanna, E., Harig, C., Helm, V., Horvath, A., Horwath, M., Khan, S., Kjeldsen, K.K., Konrad, H., Langen, P., Lecavalier, B., Loomis, B., Luthcke, S., McMillan, M., Melini, D., Mernild, S., Mohajerani, Y., Moore, P., Mouginot, J., Moyano, G., Muir, A., Nagler, T., Nield, G., Nilsson, J., Noel, B., Otosaka, I., Pattle, M.E., Peltier, W.R., Pie, N., Rietbroek, R., Rott, H., Sandberg-Sørensen, L., Sasgen, I., Save, H., Scheuchl, B., Schrama, E., Schröder, L., Seo, K.W., Simonsen, S., Slater, T., Spada, G., Sutterley, T., Talpe, M., Tarasov, L., Van De Berg, W.J., Van Der Wal, W., Van Wessem, M., Vishwakarma, B.D., Wiese, D., Wouters, B., 2018. Mass balance of the Antarctic Ice Sheet from 1992 to 2017. Nature 558 (7709), 219–222. https://doi.org/10.1038/s41586-018-0179-y.

Siegert, M.J., Ross, N., Le Brocq, A.M., 2016. Recent advances in understanding Antarctic subglacial lakes and hydrology. Philos. Trans. R. Soc. A Math. Phys. Eng. Sci. 374 https://doi.org/10.1098/rsta.2014.0306.

Smith, A.M., Bentley, C.R., Bingham, R.G., Jordan, T.A., 2012. Rapid subglacial erosion beneath Pine Island Glacier, West Antarctica. Geophys. Res. Lett. 39, 1–5. https://doi.org/10.1029/2012GL051651.

Sommers, A., Meyer, C., Morlighem, M., Rajaram, H., Poinar, K., Chu, W., Mejia, J., 2023. Subglacial hydrology modeling predicts high winter water pressure and spatially variable transmissivity at Helheim Glacier, Greenland. J. Glaciol. 1–13 https://doi.org/10.1017/jog.2023.39.

Stearns, L.A., Smith, B.E., Hamilton, G.S., 2008. Increased flow speed on a large East Antarctic outlet glacier caused by subglacial floods. Nat. Geosci. 1 (12), 827–831. https://doi.org/10.1038/ngeo356.

Werder, M.A., Hewitt, I.J., Schoof, C.G., Flowers, G.E., 2013. Modeling channelized and distributed subglacial drainage in two dimensions. Case Rep. Med. 118, 2140–2158. https://doi.org/10.1002/jgrf.20146.

Willis, I.C., Pope, E.L., J-mc Leysinger Vieli, G., Arnold, N.S., Long, S., 2021. Drainage Networks, Lakes and Water Fluxes Beneath the Antarctic Ice Sheet. https://doi.org/10.1017/aog.2016.15.

Wu, Zhen, Zhang, Huiwen, Liu, Shiyin, 2021. Dynamic process simulation of a glacier on Qilian Mountain based on a thermo-mechanically coupled model. Sci. Total Environ. 781, 147027 https://doi.org/10.1016/j.scitotenv.2021.147027 (ISSN 0048-9697).

Zwinger, T., Nield, G.A., Ruokolainen, J., King, M.A., 2020. A new open-source viscoelastic solid earth deformation module implemented in Elmer (v8.4). Geosci. Model Dev. 13, 1155–1164. https://doi.org/10.5194/gmd-13-1155-2020.